International Journal of Thermophysics (2019) 40:97
https://doi.org/10.1007/s10765-019-2564-7

An Integrated Thermal and Mechanical Performance Analysis of Effect of Cold Molten Salt Temperature for Thermocline Tank

Gang Wang[1] · Shuyang Yu[1] · Shuqun Niu[1] · Zeshao Chen[2] · Peng Hu[2]

Received: 8 June 2019 / Accepted: 9 October 2019 / Published online: 6 November 2019
© Springer Science+Business Media, LLC, part of Springer Nature 2019

Abstract

To study the effect law of cold molten salt temperature on both the thermal energy storage and mechanical performances of a thermocline molten salt tank, a numerical model of the tank which includes a multi-layer wall is established. The tank wall consists of three layers, which are firebrick, steel, and ceramic, respectively. Fluent code is employed to carry out the simulations of five different complete operation cycles of the thermocline tank. An integrated thermal and mechanical performance analysis of the effect of cold molten salt temperature for the thermocline tank is carried out. The analysis results reveal that for all the simulated cases, the thermocline is steady, and both the charging and discharging processes of the tank are stable. The thermocline thickness of the charging process can be smaller than that of the discharging one. The axial temperature of steel wall does not change synchronously with the central axial temperature of molten salt during both charging and discharging processes. As the cold molten salt temperature decreases, the thermocline thickness as well as the maximum mechanical stress of the steel wall increases. Hence, it can be drawn that increasing the cold molten salt temperature properly will be of benefit to both the energy storage performance and stability of the thermocline tank structure.

Keywords CSP · Effect of cold molten salt temperature · Energy storage · Thermocline tank · Integrated thermal and mechanical analysis

Abbreviations

C_p Specific heat, $J \cdot kg^{-1}K^{-1}$
D Tank diameter, m

✉ Gang Wang
kinggang009@163.com

[1] School of Energy and Power Engineering, Northeast Electric Power University, Jilin City 132012, Jilin, China

[2] School of Engineering Science, University of Science and Technology of China, Hefei 230027, Anhui, China

D' Inner diameter of the inlet and outlet pipeline, m
E Elasticity modulus, Pa
F Inertial coefficient of the porous medium
H Height of the filling area, m
H' Height of the upper and lower distributor zones, m
h_i Interstitial heat transfer coefficient, $W{\cdot}m^{-2}K^{-1}$
K Intrinsic permeability of the porous medium, m^2
k Thermal conductivity, $W{\cdot}m^{-1}K^{-1}$
L Thickness, m
T Temperature, K
u Velocity, $m{\cdot}s^{-1}$

Greek symbols

α Thermal expansion coefficient, K^{-1}
ε_m Mechanical strain
ε_t Thermal strain
δ Thermocline thickness, m
Θ Dimensionless temperature
μ Viscosity, $kg{\cdot}m^{-1}s^{-1}$
ρ Density, $kg{\cdot}m^{-3}$
σ Principal stress, Pa
σ_{max} Maximum mechanical stress, Pa
σ_γ Yield strength, Pa

Subscripts

b Bottom
c Cold molten salt
h Hot molten salt
in Inlet
l Liquid molten salt
m Mechanical
max Maximum
min Minimum
s Solid filler
t Thermal
top Top

1 Introduction

Due to the growing focus on renewable energy resources, solar energy utilization technologies have been developed rapidly in recent years [1, 2]. Large-scale solar power cannot be widely popularized and commercialized in the world due to the intermittency, volatility, and variability with seasonal climate of solar energy [3]. Direct solar power generation technology is one of the most attractive ways to use solar energy to generate electricity [4]. For the solar thermal power

generation, advanced and efficient heat storage technology can solve the above problems existing in the solar energy utilization [5], which is conducive to the popularization of solar thermal power generation technology. Due to the advantages of molten salt in heat transfer and energy storage applications, molten salt is selected as the heat transfer medium in primary circuit and heat storage medium in energy storage sub-system of many new concentrated solar power (CSP) plants. Currently, two-tank heat storage technology in solar thermal power plant is relatively mature, but its initial investment cost is high. In order to reduce the cost, researchers proposed the thermocline molten salt energy storage system [6]. The relevant research results show that it leads to a 35 % reduction in initial investment compared with the two-tank heat storage system. Therefore, the thermocline molten salt energy storage system has been widely concerned and studied [7].

There is a convective heat transfer process with large temperature difference thermocline in a thermocline molten salt tank. This process directly influences the heat storage and mechanical characteristics of the thermocline tank. Therefore, the study on flow and heat transfer in thermocline tank is of great significance. Many researchers have carried out a series of studies on heat storage performance of thermocline tank.

Pacheco et al. [8] developed a thermocline tank using molten-nitrate salt and relevant experiments on thermal cycling of the tank were carried out. The circulation operation of molten salt thermocline tank was simulated and the effect of internal particle diameter and external convection loss on tank performance was studied by Flueckiger and Garimella [9]. Angelini et al. [10] established a two-dimensional numerical model for the packed-bed thermocline molten salt energy storage system and made a comparison between the simulation results and practical efficiency of a two-tank heat storage system. It was found that the heat storage efficiency of the thermocline tank was about 65 %. Bayon and Rojas [11] developed a single-phase one-dimensional model called CIEMAT1D1SF to simulate a thermocline thermal storage system. The evaluation of effect of dimensionless velocity on the thermocline thickness and tank efficiency was launched. The operation strategy of thermocline tank was studied by Biencinto et al. [12]. The results show that the optimal single tank operation strategy was to retain part of the thermocline area in the tank during the charging process and the tank was completely emptied during the discharging time. Hoffmann et al. [13] conducted a comparison study between the experimental and simulation results of different scale thermocline tanks. The sensitivity study on different numerical models was also carried out. In general, though some parameters influencing the energy storage performance of thermocline tank were investigated, there is still a lack of the effect evaluation of cold molten salt temperature on both the thermal and mechanical performances of thermocline tank.

To fill the research gap mentioned above, this paper carries out an integrated thermal and mechanical performance analysis of the effect of cold molten salt temperature for thermocline tank. The numerical model of a thermocline molten salt tank with a multi-layer wall (composed of firebrick, steel wall and ceramic) is established. Five different cases of complete operation cycle of the thermocline tank are simulated. The effect laws of cold molten salt temperature on heat storage performance

and mechanical stress are studied, which can provide a theoretical basis for the design and operation control for the thermocline molten salt heat storage system.

2 Physical Model

The research object of this paper is a thermocline tank with high-temperature molten salt as the heat transfer and storage mediums. It is widely used as the energy storage sub-system in the parabolic trough CSP generation system. The schematic diagram of the tank is illustrated in Fig. 1 [14]. The central part of the tank is filled with the porous medium. The height of the filling area H is 10.0 m, and the tank diameter D is 5.0 m. The heights of the inlet and outlet pipelines are both 1.0 m. The inner diameter D' of the inlet and outlet pipelines is 1.0 m. The height H' of the upper and lower distributor zones is assumed to be 1.0 m. The tank wall is complex and consists of the firebrick, steel wall, and ceramic successively from inside to outside. The thicknesses of the three wall layers are $L_n = 0.1$ m, $L_g = 0.02$ m, and $L_t = 0.05$ m, respectively.

A complete operation cycle of the thermocline molten salt tank includes the charging and discharging processes. In the charging process, the molten salt is heated by the solar energy receiver first and then enters the tank from the upper entrance of the thermocline tank, contacting with the low-temperature molten salt to form the thermocline. The thermocline moves downward and the low-temperature molten salt flows out from the bottom of the tank. Thus, the high-temperature molten salt is stored in the tank. The discharging process of the thermocline tank is just opposite. The low-temperature molten salt enters the tank from the lower inlet of the tank. The high-temperature molten salt originally stored in the tank moves upward and flows out of the tank top, while the low-temperature molten salt is stored in the tank.

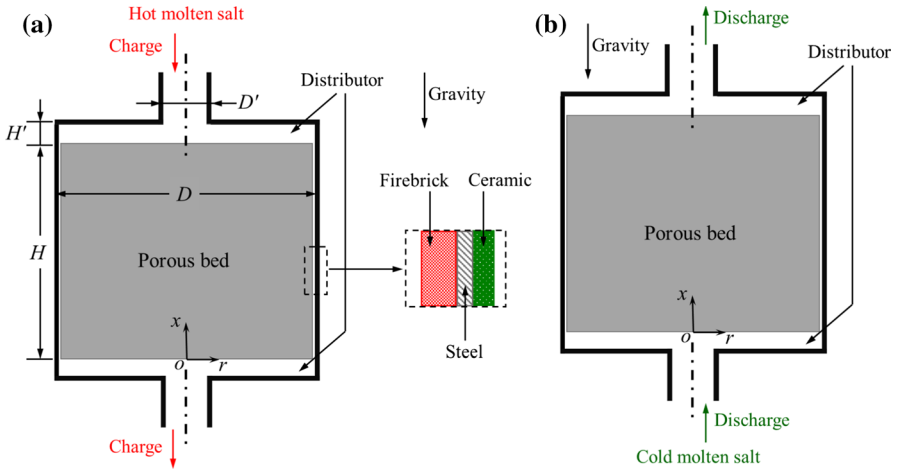

Fig. 1 Schematic diagram of the thermocline tank with complex wall [14]: (a) charging process, (b) discharging process

The thermocline thickness is a commonly used indicator which evaluates the thermal stratification efficiency of the thermocline tank. It can be described by using a dimensionless temperature Θ, which is expressed as [15]

$$\Theta = \frac{T_l - T_c}{T_h - T_c}, \tag{1}$$

where T_l is the molten salt temperature at a certain location in the thermocline area. T_c stands for the temperature of the inlet cold molten salt during the discharging process. T_h represents the temperature of the inlet hot molten slat during the charging process. As illustrated in Fig. 2, the thermocline thickness δ is normally considered to be the axial distance between the two lines where the dimensionless temperatures are 0.06 and 0.94, respectively. Equation 1 can be used when the thermocline is between the top and bottom lines of the molten salt tank (see H_{top} and H_b in Fig. 2). A more intuitive formula to define the thermocline thickness is as follows [16]:

$$\delta = \begin{cases} H_{crit,h} - H_{crit,l} & \left(T_b \le T_{crit,l} \text{ and } T_{top} \ge T_{crit,h}\right) \\ H_{crit,h} - H_b & \left(T_b > T_{crit,l}\right) \\ H_{top} - H_{crit,l} & \left(T_{top} < T_{crit,h}\right) \end{cases}, \tag{2}$$

where $T_{crit,l}$ is the molten salt temperature at the location where the dimensionless temperature Θ is 0.06, and $H_{crit,l}$ is the tank axial height corresponding to $T_{crit,l}$. $T_{crit,h}$ is the molten salt temperature at the location where Θ is 0.94, and $H_{crit,h}$ is its corresponding tank axial height. T_{top} and T_b are the molten salt temperatures at the top and bottom locations of the thermocline tank, respectively. For Eq. 2, the first formula on the right can be used when the thermocline is between the top and bottom lines of the tank for both the charging and discharging processes. The second one on the right is used when the thermocline starts to flow out of the tank during the

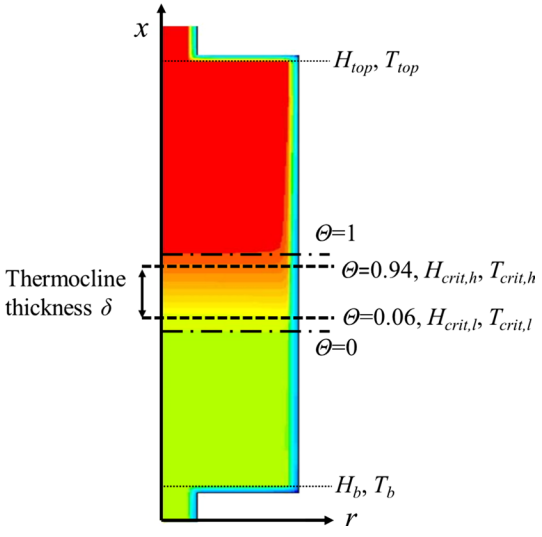

Fig. 2 Schematic diagram of the thermocline thickness

charging process. The third one is used when the thermocline starts to flow out of the tank during the discharging process.

3 Numerical Modeling and Materials

3.1 Governing Equations

In this study, the simulation assumptions are as follows: The inlet of the thermocline molten salt tank is a uniform velocity inlet condition. The heat transfer fluid is incompressible. No internal heat source exists. The filled porous medium in the thermocline tank is isotropic. The convective heat transfer boundary condition is adopted on the inner wall of the tank. Both convection and radiation heat transfer processes between the tank and the surrounding atmosphere are considered. For the convenience of simulation, the computational domain is divided by the central line and half of the thermocline tank is taken into account, as shown in Fig. 3.

Based on the model presented in Fig. 3, the governing equations involved in the operation of the thermocline tank are listed below [17].

The continuity and momentum equations of the liquid molten salt are

$$\frac{\partial\left(\varepsilon\rho_l\right)}{\partial t}+\nabla\cdot\left(\rho_l\bar{u}\right)=0 \tag{3}$$

$$\frac{\partial\left(\rho_l\bar{u}\right)}{\partial t}+\nabla\cdot\left(\rho_l\frac{\bar{u}\bar{u}}{\varepsilon}\right)=-\varepsilon\nabla\cdot p+\nabla\cdot\bar{\bar{\tau}}+\varepsilon\rho_l\bar{g}+\varepsilon\left(\frac{\mu}{K}+\frac{F}{\sqrt{K}}\rho_l|\bar{u}|\right)\bar{u}, \tag{4}$$

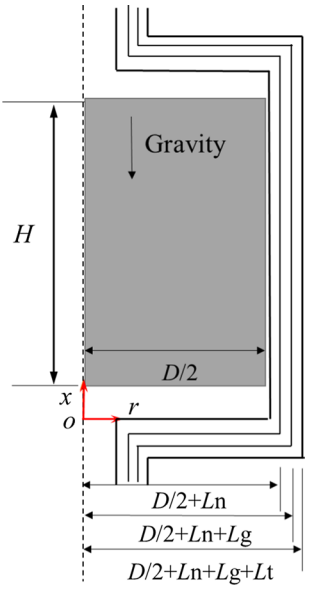

Fig. 3 Mathematical model for the simulation of the thermocline tank

where K and F represent the intrinsic permeability and inertial coefficient of the porous medium in the thermocline tank, respectively. ε stands for the porosity of the porous bed.

The energy equation of the molten salt is

$$\begin{aligned}&\frac{\partial\left[\varepsilon\rho_l C_{P,l}\left(T_l-T_c\right)\right]}{\partial t}+\nabla\cdot\left[\rho_l\bar{u}C_{P,l}\left(T_l-T_c\right)\right]\\&=\nabla\cdot\left(k_e\nabla T_l\right)-p\nabla\cdot\bar{u}+\mathrm{tr}\left[\nabla\left(\frac{\bar{u}}{\varepsilon}\right)\cdot\bar{\bar{\tau}}\right]+\frac{\bar{u}\cdot\bar{u}}{2\varepsilon}\times\frac{\partial\rho_l}{\partial t}+h_i\left(T_s-T_l\right)\end{aligned},\tag{5}$$

where T_s represents the temperature of solid filling medium in the thermocline tank. T_c stands for the temperature of cold molten salt at the lower entrance of the tank. k_e represents the effective thermal conductivity of liquid molten salt. h_i represents the interstitial heat transfer coefficient between the molten salt and filling medium in the tank.

The energy equation of the solid filling medium is

$$\frac{\partial}{\partial t}\left[(1-\varepsilon)\rho_s C_{P,s}\left(T_s-T_c\right)\right]=-h_i\left(T_s-T_l\right),\tag{6}$$

where ρ_s and $C_{\mathrm{p},s}$ stand for the density and specific heat of solid filling medium, respectively.

The temperature distribution of firebrick, steel wall, and ceramic can be directly calculated by the heat conduction equation, which is not given here.

When the thermocline tank undergoes operation cycles of successive charging and discharging processes, the thermal ratcheting can occur [14]. During the charging process, as the thermocline tank heats up, the steel wall expands, and the filler particles follow that expansion and settle lower to fill the additional volume between the tank wall and porous bed. As the tank temperature decreases during the discharging process, the filler particles remain static, preventing the tank wall from shrinking. That leads to a build-up of mechanical stress in the tank shell through repeated operation cycles. The volumes of all solid materials changes in a limited way with their temperatures increased. The steel tank shell is freely retractable in the height direction and not limited by the shell structure. However, in the circumferential direction, the deformation is determined by the maximum temperature experienced at each axial position. Then it remains settled if it does not exceed the yield strength of the steel material. In this direction, the strain is composed of two parts, which are the thermal strain ε_t and mechanical strain ε_m:

$$\varepsilon_L(x,r)=\varepsilon_t+\varepsilon_m.\tag{7}$$

The thermal strain is related to the thermal expansion coefficient α of a given material:

$$\varepsilon_t(x,r)=\alpha\left[T_2(x,r)-T_{ref}\right].\tag{8}$$

According to Hooke's law, the mechanical strain is related to the elasticity modulus E and the principal stress σ of the steel:

$$\varepsilon_m(x,r) = \frac{1}{E}\left[\sigma_{11} - \nu\left(\sigma_{22} + \sigma_{33}\right)\right]. \tag{9}$$

For a specified location along the steel shell, the maximum mechanical stress σ_{max} is expressed as

$$\sigma_{\max}(x,r) = \alpha E\left[T_{2,\max}(x,r) - T_{2,\min}(x,r)\right] < \sigma_{\gamma}, \tag{10}$$

where σ_{γ} stands for the yield strength of the steel wall material of the tank.

In this study, for the mechanical analysis of steel wall, the thermal expansion coefficient, elasticity modulus, and yield strength are assumed to be 0.00 001 K^{-1}, 200.0 GPa, and 200.0 MPa, respectively.

3.2 Numerical Approach and Definite Solution Conditions

In this paper, Fluent code is used for the numerical simulation of the charging and discharging processes of the thermocline tank. The two-dimensional double precision solver and *k-ε* turbulence model are employed in the calculation. The gravity is considered. Boussinesq model is adopted to consider the buoyancy drive. The first-order upwind scheme is adopted for the discretization. The coupling calculation of pressure and velocity is achieved by using the PISO algorithm. For the grid independence verification, the number of grids in the numerical model is increased continuously. When the total number of grids is increased to about 85 000, the temperature distribution of molten salt tends to be stable, which meets the requirement of calculation accuracy. Parts of the structural parameters of the computational domain and definite solution conditions are as follows:

a. The total height and inner radius of the thermocline tank are 12.0 m and 2.5 m, respectively. The thicknesses of the firebrick, steel wall, and ceramic are 0.1 m, 0.02 m, and 0.05 m, respectively.
b. The convection and radiation heat transfer processes between the atmosphere and outer surface of the tank are considered. The convective heat transfer coefficient is 10.0 $W{\cdot}m^{-2}K^{-1}$, and the emissivity of the tank outer surface is 1.0.
c. For the charging process, the inlet molten salt temperature is 723.0 K. The inlet molten salt velocity u_{in} is 0.003 $m{\cdot}s^{-1}$. The initial temperature of cold molten salt in the tank is 566.0 K.
d. For the discharging process, the inlet molten salt temperature is 566.0 K. The inlet molten salt velocity u_{in} is 0.003 $m{\cdot}s^{-1}$. The initial temperature of hot molten salt in the tank is 723.0 K.
e. The half-cycle time is 5.69 h.

3.3 Material Parameters

In this study, it is assumed that the binary nitrate molten salt (60 wt% $NaNO_3$ + 40 wt% KNO_3) is used as the heat transfer and heat storage mediums. The expressions of the density ρ_l ($kg{\cdot}m^{-3}$), thermal conductivity k_l ($W{\cdot}m^{-1}K^{-1}$), specific

heat $C_{P,l}$ (J·kg^{-1}K^{-1}), and viscosity μ (kg·m^{-1}s^{-1}) of the molten salt are as follows [18]:

$$\rho_l = 2090 - 0.636T_l \tag{11}$$

$$k_l = 0.443 + 1.9 \times 10^{-4} T_l \tag{12}$$

$$C_{P,l} = 1443 - 0.172T_l \tag{13}$$

$$\mu = \left(22.714 - 0.12T_l + 2.281 \times 10^{-4} T_l^2 - 1.474 \times 10^{-7} T_l^3\right) \times 10^{-3}, \tag{14}$$

where T_l (°C) stands for the molten salt temperature.

The physical parameters of the solid filling medium in the thermocline tank and the tank wall materials are shown in Table 1. The equivalent diameter of the filler particles is assumed to be 0.05 m, and the porosity of the porous bed is assumed to be 0.22.

3.4 Numerical Model Verification

In order to verify the applicability of the numerical model (mainly the complex wall structure) in this paper, the experimental device parameters given in the paper of Pacheco et al. [8] are used for the modeling and comparison analysis. The simulation results are compared with the experimental results provided in Ref. [8]. Figure 4 illustrates the comparison between the numerical and experimental results of the molten salt temperature at the centerline of the tank during the discharging process. It can be seen from Fig. 4 that the numerical and experimental results have good agreements within the range of experimental uncertainty.

4 Results and Discussion

4.1 Thermal Characteristics of the Tank During a Complete Operation Cycle

The basic parameters for the simulation model are shown in Table 1. In this paper, all simulation cases start after five complete operation cycles comprised by the charging and discharging processes, which are carried out to achieve the thermally periodic behavior. Based on the parameters of Table 2, a complete operation cycle of

Table 1 Physical parameters of the packing medium and tank wall materials

Materials	Thermal conductivity (W·m^{-1}K^{-1})	Density (kg·m^{-3})	Specific heat (J·kg^{-1}K^{-1})
Filler particle	5.69	2500.0	830.0
Firebrick	1.0	2000.0	1000.0
Steel wall	60.0	8000.0	430.0
Ceramic	1.0	1000.0	1000.0

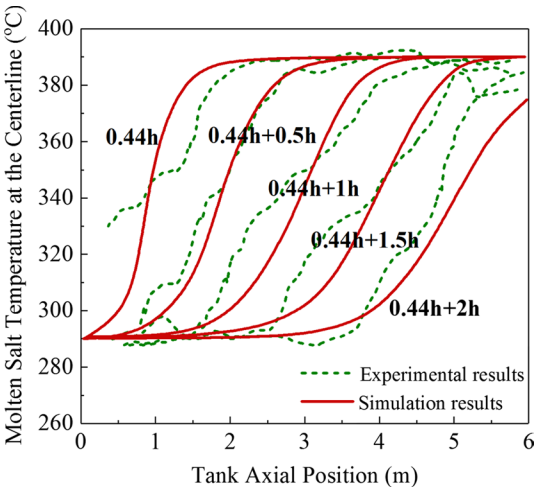

Fig. 4 Verification results of the numerical model

Table 2 Basic parameters used in the simulation model

Parameters	Values
Tank height (m)	12.0
Tank radius (m)	2.5
Inlet molten salt velocity ($m \cdot s^{-1}$)	0.003
Temperature of cold molten salt (K)	566.0
Temperature of hot molten salt (K)	723.0
Porosity of porous bed	0.22
Filler particle diameter (m)	0.05
Thermal conductivity of filler particle ($W \cdot m^{-1}K^{-1}$)	5.69
Specific heat of filler particle ($J \cdot kg^{-1}K^{-1}$)	830.0
Filler particle density ($kg \cdot m^{-3}$)	2500.0
Firebrick layer thickness (mm)	100.0
Firebrick layer density ($kg \cdot m^{-3}$)	2000.0
Specific heat of firebrick ($J \cdot kg^{-1}K^{-1}$)	1000.0
Steel wall thickness (mm)	20.0
Steel wall density ($kg \cdot m^{-3}$)	8000.0
Specific heat of steel ($J \cdot kg^{-1}K^{-1}$)	430.0
Ceramic layer thickness (mm)	50.0
Ceramic layer density ($kg \cdot m^{-3}$)	1000.0
Specific heat of ceramic ($J \cdot kg^{-1}K^{-1}$)	1000.0
Ambient temperature (K)	298.0

the thermocline molten salt tank is simulated in this section. The relevant simulation results are illustrated in Figs. 5, 6, 7, 8.

Figure 5 illustrates the thermocline thickness variations during the charging and discharging processes of a complete operation cycle. As shown in Fig. 5, for both the charging and discharging processes, the thermocline thickness increases quickly

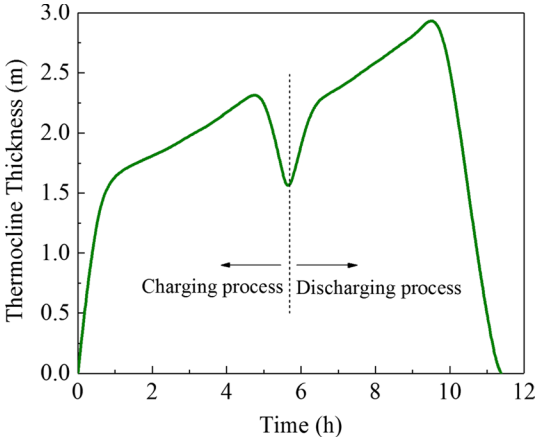

Fig. 5 Thermocline thickness variations during the complete operation cycle

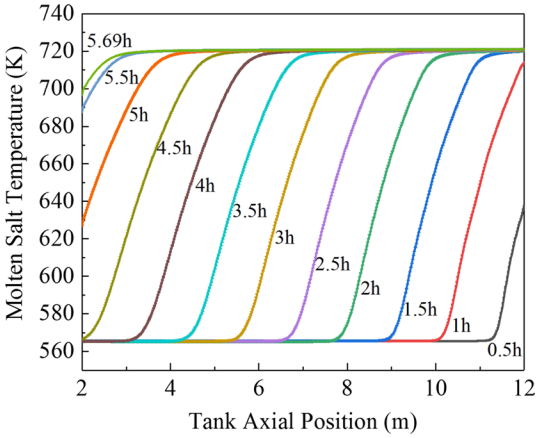

Fig. 6 Molten salt temperature variation along the tank axis during the charging process

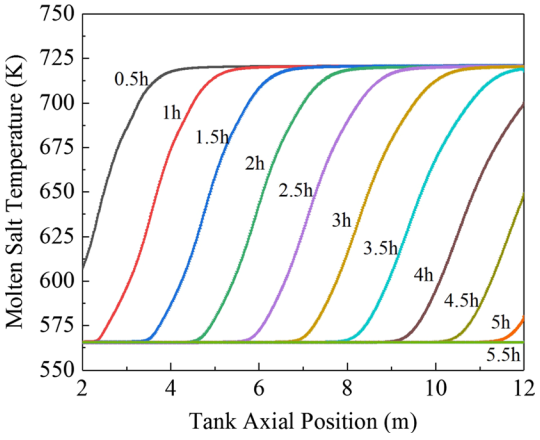

Fig. 7 Molten salt temperature variation along the tank axis during the discharging process

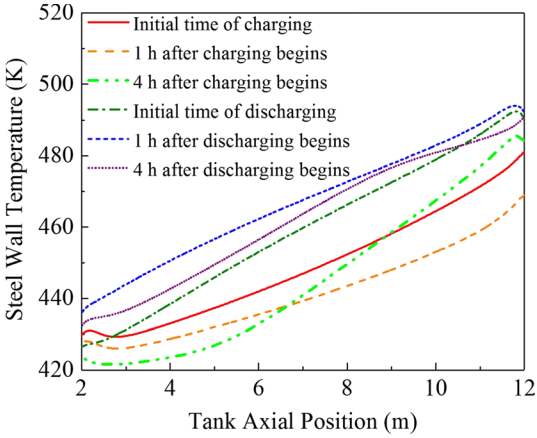

Fig. 8 Steel wall temperature variation during a cyclic operation of the thermocline tank

in the first 0.5 h. Then the increase rate of thermocline thickness slows down. The thermocline thickness starts to decrease after approximately 5.0 h of the charging process or 4.0 h of the discharging process. That means a part of the thermocline begins to leave the tank.

The molten salt temperature distributions along the axial centerline of the thermocline tank during the charging and discharging processes are presented in Figs. 6 and 7, respectively. It can be drawn from Figs. 6 and 7 that for both the charging and discharging processes, though the thermocline thickness changes over time, the thermocline shapes at different time points are close. That means the thermocline can keep relatively stable during the operation cycle of the tank.

The steel wall temperature variation during a cyclic operation of the thermocline tank is illustrated in Fig. 8. The axial temperature variation of steel wall with time forms a regular response as five complete operation cycles have been made. As illustrated in Fig. 8, during the charging process, the axial temperature of steel wall does not increase immediately with the entry of hot molten salt, and a delay in the increase of steel wall temperature exists. Similarly, the axial temperature of steel wall increases first and then decreases in the discharging process.

4.2 Effect of the Cold Molten Salt Temperature on Thermal Performance

Effect of the cold molten salt temperature on the thermal performance of thermocline tank is investigated in this section. For the initial conditions of charging processes, the temperature and flow velocity of inlet hot molten salt are 723.0 K and 0.003 $m{\cdot}s^{-1}$, respectively. As the molten salt is assumed to be 60 wt% $NaNO_3$ + 40 wt% KNO_3, it has a wide working temperature range of 473.0–723.0 K. The reference cold molten salt temperature is chosen to be 566.0 K in this study. Thus, in order to investigate a relatively wide cold molten salt temperature range and obtain obvious simulation results, the initial temperatures of cold molten salt in the thermocline tank for different simulation cases are assumed to be 506.0 K, 536.0 K, 566.0 K, 596.0 K, and 626.0 K. For the corresponding discharging processes,

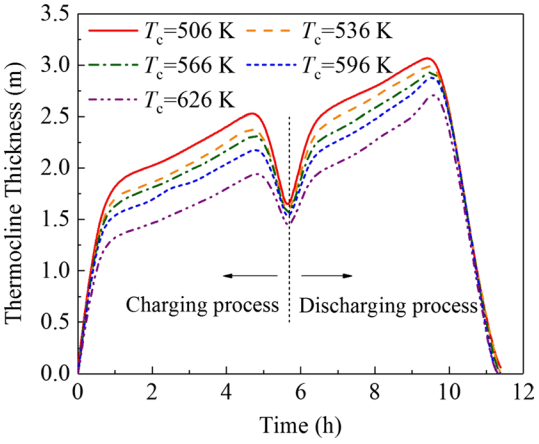

Fig. 9 Thermocline thickness variations during complete operation cycles with different initial cold molten salt temperatures

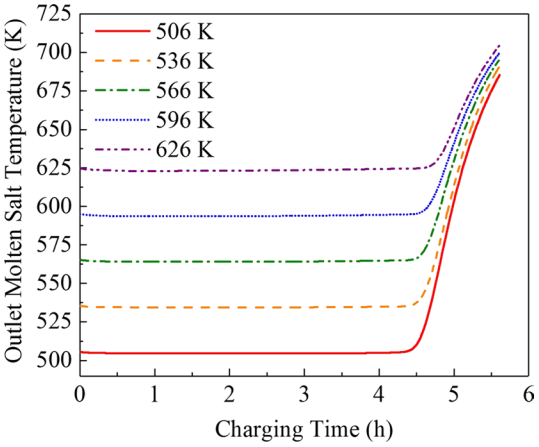

Fig. 10 Outlet molten salt temperature variations during charging processes with different initial cold molten salt temperatures

the initial temperature of hot molten salt in the thermocline tank is 723.0 K. The inlet cold molten salt temperatures are assumed to be 506.0 K, 536.0 K, 566.0 K, 596.0 K, and 626.0 K. The inlet molten salt velocity is still 0.003 $m{\cdot}s^{-1}$. The relevant simulation results are presented in Figs. 9, 10, 11.

Figures 9 and 10 present the thermocline thickness and outlet molten salt temperature variations during charging processes with different initial cold molten salt temperatures, respectively. It can be seen from Fig. 9 that total charging times of the five charging processes are nearly the same. For the same charging time point, the thermocline thickness decreases with the cold molten slat temperature increased from 506.0 K to 626.0 K. That means the thermocline thickness can be decreased by reducing the temperature difference between the hot and cold molten salts. One possible reason is that as the heat transfer temperature difference between the cold and hot molten salts increases, a greater thermocline thickness is needed to provide a greater thermal resistance, forming a relatively stable thermocline during the

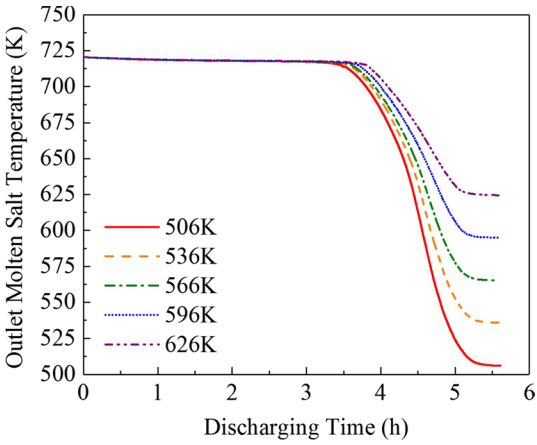

Fig. 11 Outlet molten salt temperature variations during discharging processes with different initial cold molten salt temperatures

operation process of the tank. As illustrated in Fig. 10, for the five different charging processes, though the initial temperatures of cold molten salt in the thermocline tank are different, the outlet molten salt temperatures all increase sharply after about 4.4 h of the charging processes. The maximum outlet molten salt temperature difference of the five cases is approximately 21.0 K at the end time of charging processes.

The thermocline thickness and outlet molten salt temperature variations during discharging processes with different initial cold molten salt temperatures are shown in Figs. 9 and 11. Similar to the charging processes, the increase of cold molten salt temperature leads to the decrease of thermocline thickness. But after about 4.0 h of the discharging processes, the thermocline thickness decrease caused by the increase of cold molten salt temperature is not obvious. As shown in Fig. 11, the outlet molten salt temperatures begin to decrease quickly after about 3.5 h of the discharging processes. Outlet molten salt temperature differences of the five cases at the end time of discharging processes are greater than those of the charging processes.

4.3 Effect of the Cold Molten Salt Temperature on Mechanical Performance

Mechanical performances of the thermocline tank during five operation cycles with different cold molten salt temperatures are investigated, and the relevant results are illustrated in Fig. 12. As shown in Fig. 12, for the five complete operation cycles, the peak value of maximum mechanical stress of the thermocline tank is about 143.9 MPa. With the cold molten salt temperature increased, the maximum mechanical stress at the same tank axial position decreases. That means the mechanical performance of the thermocline tank can be improved by increasing the cold molten salt temperature (or reducing the temperature difference between the hot and cold molten salts). This is because a higher cold molten slat temperature can lead to a higher steel temperature when the steel temperature reaches its minimum value during a complete operation cycle. According to Eq. 10, the maximum mechanical stress is determined by the maximum and minimum temperatures of the steel wall

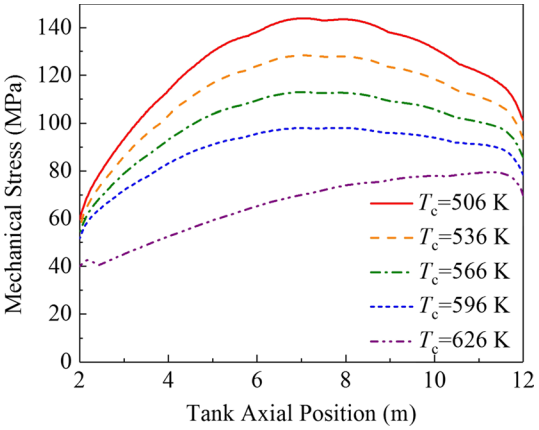

Fig. 12 Maximum mechanical stress distributions along the steel wall under different cold molten salt temperatures

during a complete operation cycle. Hence, a higher cold molten salt temperature can result in a smaller maximum mechanical stress of the steel wall.

5 Conclusions

In this study, the numerical model of a thermocline molten salt tank with multi-layer wall is established. A complete operation cycle of the thermocline tank is simulated to investigate the energy storage performance by using the CFD approach. The results reveal that the thermocline thickness increases quickly in the first 0.5 h for both charging and discharging processes. After that, the increase rate of thermocline thickness slows down. The charging process has a smaller thermocline thickness compared with the discharging one. The axial temperature of steel wall does not change synchronously with the central axial temperature of molten salt during both the charging and discharging processes. The investigation results of the effect of cold molten salt temperature on the charging and discharging characteristics show that the thermocline thickness decreases with the cold molten salt temperature increased. Thus, increasing the cold molten salt temperature properly can improve both the charging and discharging performances of the thermocline tank. The effect of cold molten salt temperature on the mechanical performance is also evaluated. The results indicate that the maximum mechanical stress decreases with the cold molten salt temperature increased. Hence, it can be drawn that the structural stability of the steel wall can be improved by increasing the cold molten salt temperature.

Acknowledgments The authors appreciate the support of the Excellent Youth Foundation of Jilin Province of China (Grant No. 20190103062JH).

References

1. G. Wang, X. Cheng, P. Hu et al., Theoretical analysis of spectral selective transmission coatings for solar energy PV system. Int. J. Thermophys. **34**, 2322–2333 (2011)

2. G. Wang, Y. Yao, Z. Chen et al., Thermodynamic and optical analyses of a hybrid solar CPV/T system with high solar concentrating uniformity based on spectral beam splitting technology. Energy **166**, 256–266 (2019)
3. S. Suman, Hybrid nuclear-renewable energy systems: a review. J. Clean. Prod. **181**, 166–177 (2018)
4. O. Farges, J.J. Bézian, M.E. Hafi, Global optimization of solar power tower systems using a Monte Carlo algorithm: application to a redesign of the PS10 solar thermal power plant. Renew. Energy **119**, 345–353 (2018)
5. S. Rodat, R. Baviere, A. Bruch et al., Dynamic simulation of a Fresnel solar power plant prototype with thermocline thermal energy storage. Appl. Therm. Eng. **135**, 483–492 (2018)
6. K.M. Powell, T.F. Edgar, An adaptive-grid model for dynamic simulation of thermocline thermal energy storage systems. Energy Convers. Manag. **76**, 865–873 (2013)
7. C. Odenthal, F. Klasing, T. Bauer, Parametric study of the thermocline filler concept based on exergy. J. Energy Storage **17**, 56–62 (2018)
8. J.E. Pacheco, S.K. Showalter, W.J. Kolb, Development of a molten-salt thermocline thermal storage system for parabolic trough plants. ASME J. Solar Energy Eng. **124**, 153–159 (2002)
9. S.M. Flueckiger, S.V. Garimella, Second-law analysis of molten-salt thermal energy storage in thermoclines. Sol. Energy **86**, 1621–1631 (2012)
10. G. Angelini, A. Lucchini, G. Manzolini, Comparison of thermocline molten salt storage performances to commercial two-tank configuration. Energy Procedia **49**, 694–704 (2014)
11. R. Bayón, E. Rojas, Simulation of thermocline storage for solar thermal power plants: from dimensionless results to prototypes and real-size tanks. Int. J. Heat Mass Transf. **60**, 713–721 (2013)
12. M. Biencinto, R. Bayón, E. Rojas et al., Simulation and assessment of operation strategies for solar thermal power plants with a thermocline storage tank. Sol. Energy **103**, 456–472 (2014)
13. J.F. Hoffmann, T. Fasquelle, V. Goetz et al., A thermocline thermal energy storage system with filler materials for concentrated solar power plants: experimental data and numerical model sensitivity to different experimental tank scales. Appl. Therm. Eng. **100**, 753–761 (2016)
14. S. Flueckiger, Z. Yang, S.V. Garimella, An integrated thermal and mechanical investigation of molten-salt thermocline energy storage. Appl. Energy **88**, 2098–2105 (2011)
15. C. Xu, Z. Wang, Y. He et al., Parametric study and standby behavior of a packed-bed molten salt thermocline thermal storage system. Renew. Energy **48**, 1–9 (2012)
16. C. Xu, Z. Wang, Y. He et al., Sensitivity analysis of the numerical study on the thermal performance of a packed-bed molten salt thermocline thermal storage system. Appl. Energy **92**, 65–75 (2012)
17. M. Fernández-Torrijos, C. Sobrino, J.A. Almendros-Ibáñez, Simplified model of a dual-media molten-salt thermocline tank with a multiple layer wall. Sol. Energy **151**, 146–161 (2017)
18. A. B. Zavoico. Solar power tower design basis document. Sandia National Laboratories. Report no. SAND2001-2100 (2001)

Publisher's Note Springer Nature remains neutral with regard to jurisdictional claims in published maps and institutional affiliations.